



Black Carbon Hot Paper

International Edition: DOI: 10.1002/anie.201914115

German Edition: DOI: 10.1002/ange.201914115

# The Molecular Composition of Soot\*\*

Rachelle S. Jacobson, Andrew R. Korte, Akos Vertes, and J. Houston Miller\*

**Abstract:** Soot (sometimes referred to as black carbon) is produced when hydrocarbon fuels are burned. Our hypothesis is that polynuclear aromatic hydrocarbon (PAH) molecules are the dominant component of soot, with individual PAH molecules forming ordered stacks that agglomerate into primary particles (PP). Here we show that the PAH composition of soot can be exactly determined and spatially resolved by low-fluence laser desorption ionization, coupled with high-resolution mass spectrometry imaging. This analysis revealed that PAHs of 239–838 Da, containing few oxygenated species, comprise the soot observed in an ethylene diffusion flame. As informed by chemical graph theory (CGT), the vast majority of species observed in the sampled particulate matter may be described as benzenoids, consisting of only fused 6-membered rings. Within that limit, there is clear evidence for the presence of radical PAH in the particulate samples. Further, for benzenoid structures the observed empirical formulae limit the observed isomers to those which are nearly circular with high aromatic conjugation lengths for a given aromatic ring count. These results stand in contrast to recent reports that suggest higher aliphatic composition of primary particles.

## Introduction

In carbon chemistry, the aromatic moiety appears in scientific disciplines as disparate as astrophysics and biochemistry. Because of the high thermodynamic stability of polynuclear aromatic hydrocarbon (PAH) molecules, these species have been identified in crude oil (including asphaltenes), are persistent organic pollutants present in many environmental soil and sediment samples, and are thought to be the source of infrared (IR) emission bands associated with many interstellar environments.<sup>[1]</sup> An additional characteristic of PAH thermodynamics is the large attractive potentials between adjacent molecular sheets ( $5 \text{ kJ mol}^{-1}/\text{C atom}$ ) and these  $\pi$ - $\pi$  interactions contribute to condensed phase structures throughout nature (e.g., DNA and protein structure).

Recent investigations, enabled by advances in both experimental and computational hardware, have revealed substantial details of the early chemistry of PAH growth as well as structural characteristics of soot<sup>[2]</sup> in flames.<sup>[3]</sup> At the beginning of the process, radical-molecule chemical mechanisms have been proposed for the formation of the first few aromatic rings, leading to condensed, largely planar, structures.<sup>[4]</sup> The physical structure of soot freshly emitted from flames has been characterized as fractal aggregates, with radii of gyration on the order of 100–400 nm, and composed of primary particles (PP) with diameters on the order of 10–50 nm.<sup>[5]</sup> Within these PP, high resolution TEM reveals disordered stacks with fringe lengths on the order of 1 nm and fringe spacing approximately that of graphite (0.35 nm).<sup>[6]</sup> Experimentally, greater challenges are presented by the intermediate stages of this process, particularly approaching the transition from two- to three-dimensional structures. Work from several laboratories has presented data from both extractive and in situ optical measurements that support our hypothesized mechanism that individual PAH molecules grow chemically until they are sufficiently large that they will agglomerate into ordered stacks and subsequently into disordered clusters. The optical results coupled with computational chemistry calculations of particle electronic properties suggest that the size of these PAHs will be approximately  $1.0 \pm 0.2 \text{ nm}$  in diameter and, on average, fall in the 450–650 Da mass range.<sup>[7]</sup> Figure 1 illustrates the processes as described above.

A limitation of recent measurements is that the results are representative of either averaged properties of the molecular ensemble comprising the particles,<sup>[8]</sup> or biased toward a subset

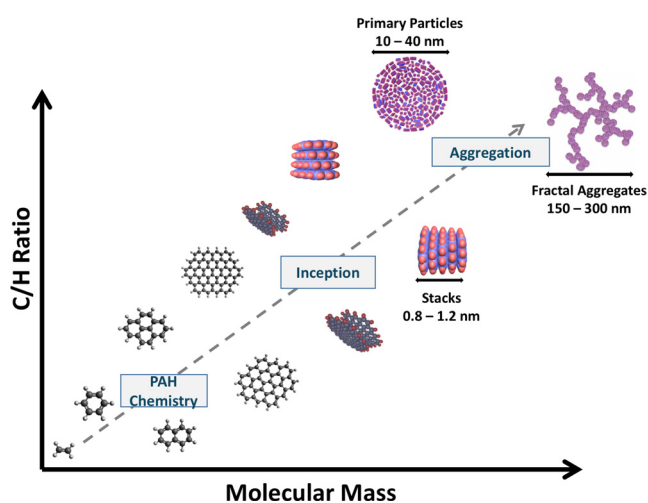


**Figure 1.** Schematic diagram of the proposed mechanism for formation of soot particulate in flames.

[\*] Dr. R. S. Jacobson, Dr. A. R. Korte, Prof. A. Vertes, Prof. J. H. Miller  
Department of Chemistry, George Washington University  
800 22<sup>nd</sup> St, NW, Suite 4000, Washington, DC 20052 (USA)  
E-mail: houston@gwu.edu

[\*\*] Reports from several groups address the ambiguity in nomenclature for soot and black carbon. The analysis reported here describes particles that most closely match the description of Buseck et al. with “ns-soot” used for carbon nanospheres of less than 100 nm in diameter. For readability, we will refer to the material analyzed as “soot”.

Supporting information and the ORCID identification number(s) for the author(s) of this article can be found under:  
<https://doi.org/10.1002/anie.201914115>.

of molecules in the distribution.<sup>[9]</sup> In this work, we use spatially-resolved laser desorption ionization-mass spectrometry (LDI-MS) to provide the first direct, detailed chemical composition of PAH molecules that comprise soot sampled from an atmospheric-pressure flame.

## Results and Discussion

The observed laser desorption ionization (LDI)—mass spectrometry (MS) spectra varied with flame position and analytical conditions. Low-fluence interrogation of samples on silicon wafer substrates yielded the most artifact-free spectra. Artifacts observed with higher fluence and on other substrates include hydrogen losses to parent ions and the formation of dimers, as verified by analysis of standard PAH samples. A spectrum acquired under these conditions 20 mm above the burner surface in the wing of the flame is shown in Figure 2A. This flame area is positioned between the region rich in hydrocarbon intermediates formed directly from the fuel ethylene<sup>[10]</sup> and the high-temperature, radical-rich region.<sup>[1]</sup> The highest particulate concentrations are observed in these annular regions at this flame height, here illustrated by measured laser-induced incandescence profiles of soot (Figure 2B).<sup>[11]</sup>

Prior laser-based MS measurements resulted in only carbon cluster ions being detected at higher  $m/z$  mass range observed in high BC regions.<sup>[12]</sup> Our PAH distribution is

centered at higher mass values than previously reported molecular beam mass spectrometry (MBMS) or early laser microprobe mass spectrometry (LMMS) results. In addition to the sampling method, the two most significant differences between the current study and others are the low laser fluence ( $3.2 \text{ mJ cm}^{-2}$ ) combined with a more sensitive, higher resolution imaging mass spectrometer. In one past report, substantially higher fluences ( $> 40 \text{ mJ cm}^{-2}$ ) were needed to generate sufficient ion signal for detection.<sup>[13]</sup> Additionally, only one insertion of the sample substrate was required to generate sufficient ion signal in the current study, potentially decreasing the contamination by other flame areas resulting from repeated insertions.

The high mass resolving power afforded by the Orbitrap analyzer allows for the resolution of nearly isobaric species. This, combined with internal calibration of the spectra to previously identified PAH ions, allows for the confident assignment of molecular formulae based on accurate  $m/z$  measurements. The assigned molecular formulae are predominantly hydrocarbon species, with comparatively few oxygenated species detected. The potential incorporation of oxygen within PAH molecules is of significant interest, particularly with regard to their environmental consequences.<sup>[14]</sup> In this study, while a small number of low-abundance ions in some flame areas could potentially be assigned as oxygenated PAH, they were very weakly detected ( $< 5\%$  relative abundance) and did not show coherent spatial distributions corresponding to the physical flame shape and

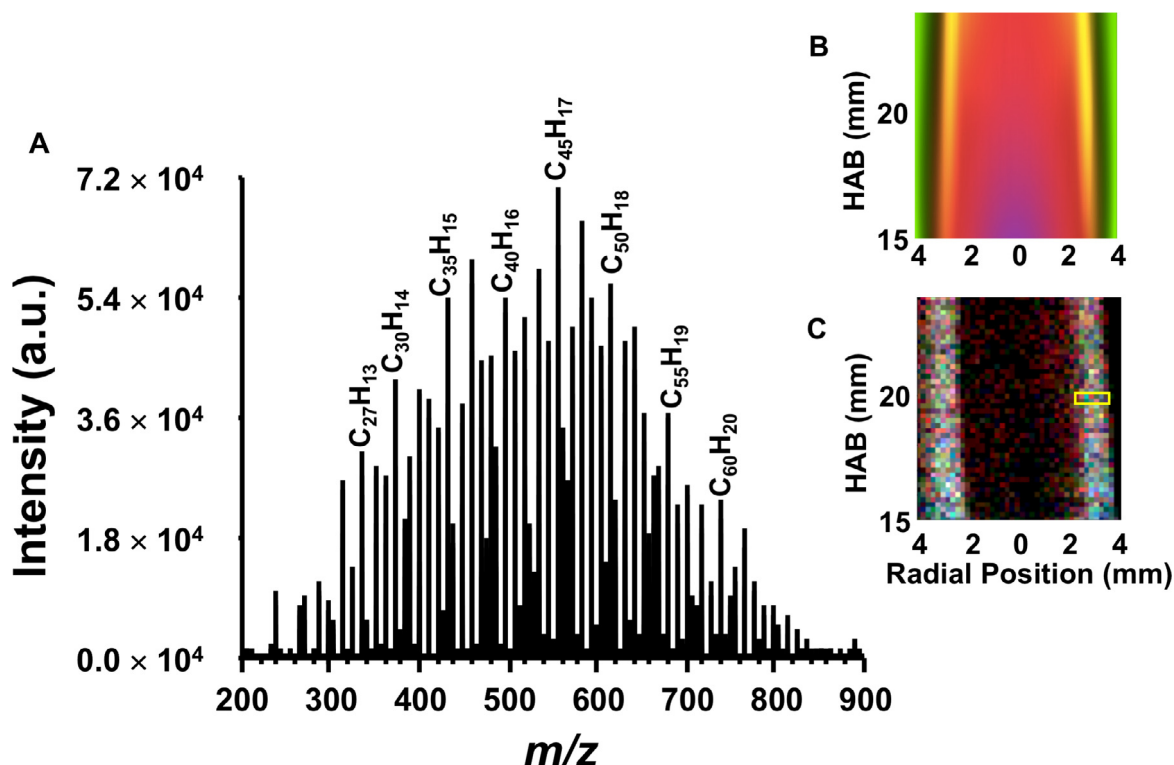


**Figure 2.** A) Representative mass spectrum from 20 mm above the burner in the flame wing; B) computed contours of ethylene (magenta), acetylene (red), and hydrogen atom concentrations (green) as well as experimental profiles of laser induced incandescence (LII-blue) (1) near base of flame. C) Mass spectral ion intensity image of  $\text{C}_{28}\text{H}_{14}^+$  (red),  $\text{C}_{42}\text{H}_{16}^+$  (green),  $\text{C}_{50}\text{H}_{18}^+$  (blue). Mass spectrum reported in part (A) collected in region outlined by a yellow box.

thus may be background- or noise-related. Flames where oxygenated-aromatic species have been identified have been burned in a premixed configuration, where the oxygen availability during molecular growth is typically much greater, or in oxygen-rich (and high temperature) regions of counter-flow diffusion flames where phenols, ethers, and furan-embedded species have been observed.<sup>[15]</sup>

Spectra acquired from the annular region 20 mm above the burner revealed a symmetric distribution of PAH ions around the flame's centerline and were comprised entirely of singly-charged ions. The arithmetic mean mass of these PAH molecules was 534.7 Da, whereas the mean weighted by absolute ion intensity was 535.6 Da, confirming the symmetric peak distribution. PAHs detected at this flame position ranged in mass from 239.0855–801.1638 Da. Mean PAH  $m/z$  and  $m/z$  ranges for other flame regions are shown in Table 1.

**Table 1:** Summary of  $m/z$  values across a series of specific flame locations. Values included in this tabulation were present in all three replicates measured, and intensities were averaged across replicates.

Flame Position		Arithmetic mean	Weighted mean	Minimum $m/z$	Maximum $m/z$
HAB 20	left wing	533.8	545.0	239.0855	838.1716
	centerline	350.1	350.1	350.1090	350.1090
	right wing	534.7	535.6	239.0855	801.1638
HAB 25	left wing	534.6	530.6	239.0855	801.1638
	centerline	479.6	466.6	276.0934	679.1481
	right wing	541.7	534.4	239.0855	814.1716
HAB 30	left wing	540.4	523.1	239.0855	805.1951
	centerline	509.7	482.9	239.0855	779.1794
	right wing	529.3	519.7	239.0855	764.1560
HAB 35	left wing	521.7	517.2	300.0934	764.1560
	centerline	557.6	541.9	239.0855	827.1794
	right wing	474.0	473.1	276.0934	681.1638

Figure 2C shows the spatial distribution of three ions within the lower, annular (wing) flame region:  $C_{28}H_{14}^+$  (red),  $C_{42}H_{16}^+$  (green),  $C_{50}H_{18}^+$  (blue). These molecules most likely correspond to benzocoronene, circumpyrene, and a seventeen-ring structure with many possible isomers. While the larger  $C_{42}H_{16}^+$  and  $C_{50}H_{18}^+$  molecules are more localized to the flame wing area, the smaller  $C_{28}H_{14}^+$  is detectable in the inner flame region as well. The yellow box indicates the pixels averaged to produce the spectrum shown in Figure 2A. It can be seen from this spectrum that at this position, there are both odd- and even-carbon numbered PAH identified in the spectrum, though in other laser-based studies, even-carbon numbered PAH dominate the spectrum.<sup>[15]</sup> In work by Homann, PAH ions that were sampled directly from a flame without being separately ionized also showed similar distributions of intensities between odd- and even-carbon numbered PAH.<sup>[16]</sup>

At height above burner (HAB) = 20 and 25 mm, high PAH ion intensities are observed in the flame wing area, near the boundary between fuel and air. This distribution is consistent with profiles produced using other experimental

techniques as well as direct numerical simulation of this flame (Figure 2B). Conversely, along the centerline the ion abundance from PAH molecules increases as the HAB is increased. Compared with the annular region, we observe a shift in  $m/z$  range to lower molecular weight PAH species in the central flame area at HAB = 25–30 mm with a narrower distribution of molecular size. At HAB = 25 mm and below, in situ measurements of soot volume fraction are unable to measure particulate near the centerline of the flame. The lack of larger PAH molecules in the center is likely the result of lower localized abundance of species critical to PAH growth, such as hydrogen atoms (shown in Figure 2B) or other relevant small radical hydrocarbons.

A comprehensive view of PAH molecules observed at different flame positions is shown in Figure 3, with a summary of the mass distribution statistics presented in Table 1. As can be seen from this plot, the flame areas with the greatest overall ion abundances correspond well with other measurements of soot particulate by in situ techniques. It is also apparent that ions with the greatest abundance are similarly distributed between even- and odd-carbon numbered PAH. In all the plots shown in Figure 3, there is a nearly normal distribution of peaks with a given number of hydrogens as the number of carbons is varied. This trend is similar to Homann's observations from native MS measurements of PAH in a low pressure flame, where these distributions were compared with structures that, in the authors' words, were "the maximally condensed arrangement of aromatic rings".<sup>[16]</sup>

Another important observation is the high concentrations of odd-carbon numbered PAH in most flame areas, especially as the soot volume fraction increases. PAH containing an odd number of hydrogen atoms, without side chains, are usually free radicals. It is possible that their observation is a sampling artefact, but there is precedence for their observation in analogous measurements.<sup>[13,17]</sup> Odd-carbon and odd-electron PAH are often fully benzenoid, although possible structures may incorporate 5-membered ring(s) or an ethynyl side chain into the structure. For example, the most likely molecular structure of  $C_{47}H_{17}$  is a fully peri-condensed 16-ring system, with one possible isomer shown in Table S1.

Additional insight into PAH structures is offered by comparing the observed distributions with two limits of PAH structure in common use in the literature: cata- and peri-condensed PAH. In a classic definition reported by Birks,<sup>[18]</sup> cata-condensed PAH are those in which no carbon atom is shared by more than two aromatic rings. Further, these structures are given the empirical formula  $C_{(4i+2)}H_{(2i+4)}$ , where  $i$  is the number of aromatic rings. Examples of cata-condensed PAH include the acenes, the phenacenes, and many highly-branched ring structures such as the acenographynes.<sup>[19]</sup> The cata-condensed limit is shown as the dashed line in the distribution plots shown in Figure 3. Peri-condensed PAH allow for carbon atoms to be shared by more than 2 rings, and this class of molecules plays a role in structures of many carbon-based materials including fullerenes, nanotubes, nano-

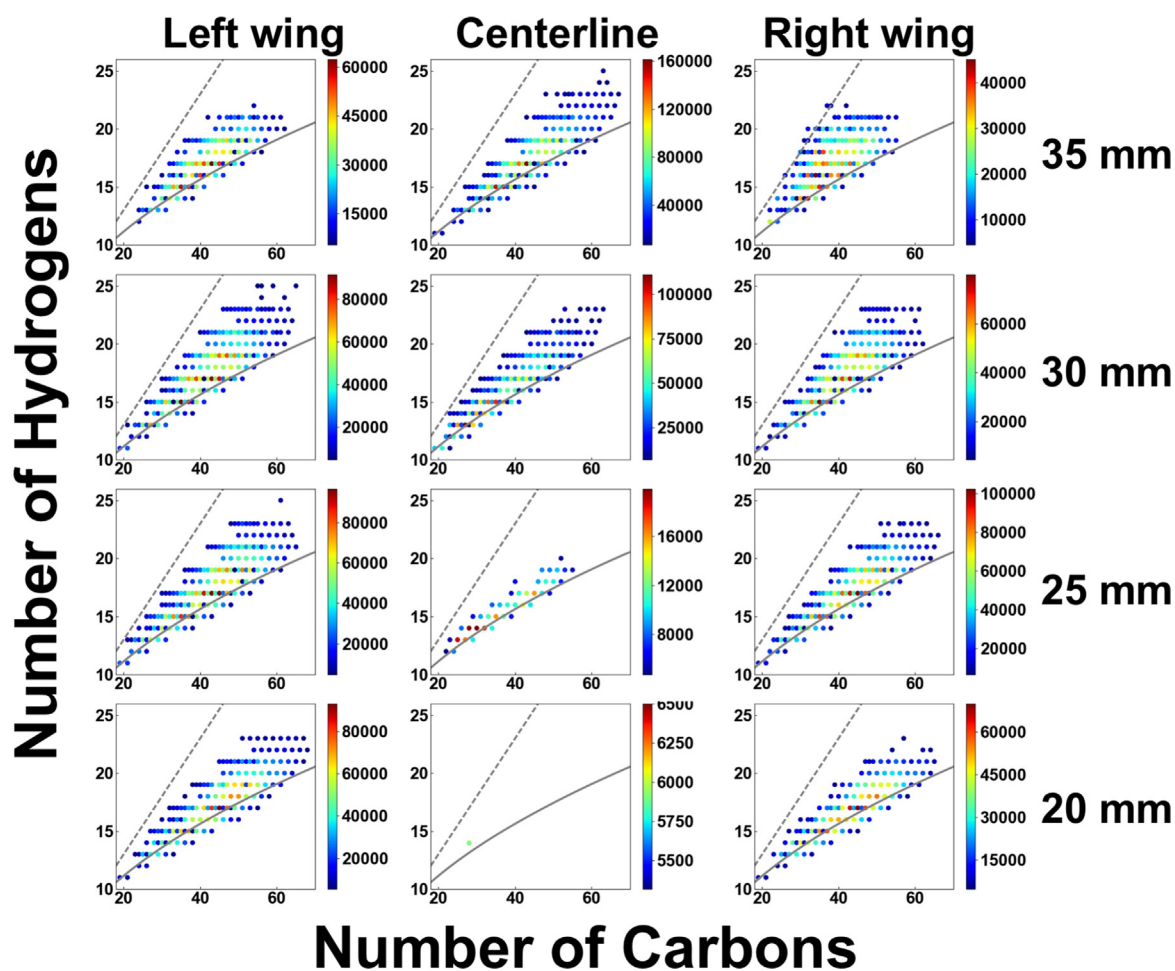


**Figure 3.** Distribution of PAH at four heights above the burner and three radial locations. Values included were present in all three replicates measured and intensities were averaged across replicates. The coloration of each plot corresponds to the averaged absolute intensity of each ion in that flame area. Also shown are C/H correlations for cata-condensed (dashed) and peri-condensed (solid) PAH structures. A map of the sampling locations is shown in Figure S2.

flakes, graphene, and graphite. The “maximally-condensed” molecules referenced by Homann comprise a homologous series of peri-condensed species with 6 free edges and varying lengths of “zig-zag”<sup>[7a]</sup> edges joining them. This series is shown in the distribution plots of Figure 3 as solid lines. Observed species that are below this peri-condensed curve may represent structures with 5-membered rings<sup>[20]</sup> or ethynyl side chains added to peri-condensed PAHs. In their high resolution AFM study of soot, Commodo et al.<sup>[20c]</sup> report both PAH with five-membered rings as well many PAH with aliphatic branches, predominantly methyl groups, although they note the presence of  $sp^3$  methylene groups in some of the penta rings.

There are some notable differences in both flame system and sampling protocol between the present study and the Commodo et al. reference.<sup>[20c]</sup> The distributions revealed in our LDI-MS experiments lie much closer to the highly-condensed limit than the cata-condensed line. Further, the presence of side chains with  $sp^2$  or  $sp^3$  bonded carbons would only shift species’ empirical formulae to lower C/H ratios, which is not supported by this data.

Another approach for teasing out structural insight about the collected particulate is available from chemical graph theory (CGT). The connections between graph theory and chemical structure and isomer enumeration date to the mid-19th century and are often attributed to the English mathematician Cayley.<sup>[21,22]</sup> In the ensuing 150 years, quantum models for atomic and molecular electronic structure emerged and were subsequently validated by spectroscopy, computational chemistry, and even atomic scale imaging. Mathematicians and chemists have returned to the topic repeatedly and have continued to find the formalisms of CGT valuable in rationalizing observed properties at every molecular scale. Perhaps because of its intimate connection with hexagonal tiling, no chemical bonding category has received more attention than the structure of polynuclear aromatic hydrocarbons. (The reader is referred to the essential review of Randić<sup>[22]</sup>) Throughout this rich history, Kekulé, Hückel, Pauling, and Clar<sup>[7a]</sup> have often been recognized for their contributions to the understanding of aromatic structure.

Over the last several decades, the work of Dias<sup>[23]</sup> and Brunvoll and Cyvin<sup>[24]</sup> should also be recognized for their extensive contributions to the application of CGT to our

understanding of PAH bonding and structure. Using the mathematical tools developed in these references, important limits emerge to confine the structure of molecules observed in the data obtained in the current experiments. As an example, we consider one of the mass spectra collected at 35 mm HAB in the wings of the flame. In this spectrum, there are approximately 180 identified  $m/z$  peaks (with intensities between 4200 and 86000). The vast majority of these have empirical formulae consistent with fully benzenoid hydrocarbons. Specifically, for a hydrocarbon of formula  $C_nH_s$ , benzenoid species will satisfy where quantities within the curly brackets [Eq. (1)] are rounded up to the nearest integer.

$$2 \left\{ \frac{1}{2} (n + \sqrt{6n}) \right\} - n \leq s \leq n + 2 - 2 \left\{ \frac{1}{4} (n - 2) \right\} \quad (1)$$

Since the seminal work of Stein and Fahr<sup>[25]</sup> that defined the most thermodynamic structure for a molecule with a given inventory of carbon and hydrogen atoms, there has been nearly continuous debate about whether molecular growth is thermodynamically vs. kinetically limited. The consensus is that it may have elements of both in the sense that radical-initiated growth chemistry leads to larger, and more stable benzenoid PAH.<sup>[26]</sup> However, more recent literature suggests the importance of PAH structures which include five-membered rings. When either one (fluoranthenoids) or two (indacenoids) five membered rings are included in a PAH structure, the number of possible isomers increases dramatically,<sup>[27]</sup> indicative of the statistically greater ways to produce these structures from smaller PAH. This conjecture has been borne out using the kinetic Monte Carlo variant known as stochastic nanoparticle simulator (SNAPS), which tracks the growth of individual PAH where reactivity is informed by atom type, bonding environment, and steric considerations. When applied to PAH growth chemistry, SNAPS produces many PAH with five-membered rings,<sup>[28]</sup> both at the PAH periphery and embedded in six-membered rings. Further, PAH with five-membered rings have been observed in samples drawn from low-pressure flames.<sup>[29]</sup> Nonetheless, the consensus is that PAH with five-membered rings are not as stable as fully benzenoid structures<sup>[27]</sup> and it has been shown that interior carbon atoms in benzenoids are substantially more chemically inert than interior carbons in curved PAH (which occur with embedded five-member rings structures).<sup>[30]</sup>

For benzenoid structures, Brunvoll and Cyvin<sup>[24]</sup> provide a great deal of additional limitations on and insights into structures based solely on empirical formula. For example, relationships are drawn for the number of internal carbon atoms,  $n_i$ ; the number of hexagonal rings,  $h$ ; and the numbers of isomers, both Kekuléan (closed shell) and non-Kekuléan (radicals). Finally, they provide an extensive discussion on what they refer to as the Dias Parameter,  $d_s$ , suggested by Dias to be a count of tree disconnections where “trees” are constructed from lines connecting internal carbon atoms. Brunvoll and Cyvin<sup>[24]</sup> show how the Dias parameter can be calculated directly from the empirical formula  $C_nH_s$  from [Eq. (2)]:

$$d_s = \frac{1}{2} (3s - n) - 7 \quad (2)$$

The Dias Parameter is 0 when there are no disconnections, positive when there are, and negative for branched trees which occur when there are extensive networks of interior carbons. As an example, consider several 6-ring molecules which were observed in our mass spectra:  $C_{24}H_{12}$  (coronene),  $C_{25}H_{13}$ ,  $C_{26}H_{14}$ ,  $C_{27}H_{15}$ . All of the isomers of the odd-carbon species are radicals (as well as a small number of the isomers of the even-carbon species). The number of possible isomers (1, 3, 10, and 5, respectively<sup>[31]</sup>) grows with  $d_s$  (-1, 0, 1, and 2) while it is observed that the MS intensity is greater for the low  $d_s$  molecules (10365, 26997, 5226, and 8558, respectively) despite the statistically smaller number of structures that satisfy the empirical formula for low  $d_s$ . The same trends are seen for groups containing higher numbers of rings observed in our spectra (See Supporting Information, Figure S3).

The Dias parameter may also be viewed in the context of other measures of bonding and stability in aromatic molecules that have appeared over the last several decades including the work of Stein and Fahr<sup>[25]</sup> as well as structural classifications based on the work of Clar.<sup>[3]</sup> Specifically, compact, nearly circular structures will have the lowest  $d_s$ , the greatest number of aromatic sextets, and are also the most thermodynamically stable (Figure S4).

Our results challenge observations of some recent experiments as well as proposed models for incipient particle structure in which incipient particles are suggested to have both aromatic and aliphatic carbon bonding.<sup>[32]</sup> In a recent contribution by Johansson et al., the authors propose a mechanism for the inception of particles (clustering of hydrocarbons by radical-chain reactions, CHRCCR) that form incipient particles with aromatic islands connected by aliphatic side chains<sup>[32b]</sup> surrounding a highly branched, large central molecule. They further propose that these incipient particles serve as active sites for chemisorption of small hydrocarbons that would lead to PP with more aliphatic than aromatic surface character. We did not observe “seed” molecules with structures similar to that proposed by the CHRCCR mechanism in this study. However, we cannot rule out the possibility that these molecules exist in concentrations too low to be detectable by our protocol.

The contradiction between our current results and those suggesting more aliphatic composition of primary particles remains an important topic for continued investigations. One of the motivations for the development of the CHRCCR model was the lack of experimental evidence for sufficiently high concentrations of large monomer PAH in flames to explain observed primary particle concentrations, a conclusion made by us in an early calculation of the equilibrium constant for the dimerization constant for PAH.<sup>[33]</sup> In subsequent publications, we qualified this conclusion by noting that sufficiently large PAH will physically condense at temperatures characteristic of soot formation in diffusion flames.<sup>[26b]</sup> Several recent studies have placed the limit for the physical agglomeration of PAH at sizes even larger (> 700 Da) than observed here.<sup>[34]</sup> This has led to suggestions that more complex chemistry may play a role in in PP formation including

aromatic excimer formation<sup>[35]</sup> (perhaps with aliphatic linkages<sup>[36]</sup>) through radical<sup>[37]</sup> (or diradicals<sup>[38]</sup>), or “rim-bonding”.<sup>[39]</sup> The data presented here, as well as in contemporary studies showing evidence for PAH clustering,<sup>[40]</sup> provides proof that species of sufficient size are present and that their size is consistent with the conjugation length inferred by both Raman scattering and optical band gap measurements observed in the same burner/flame system.<sup>[7b,8]</sup>

## Conclusion

In this article we have presented the results of low-fluence, laser desorption ionization, coupled with high-resolution mass spectrometry analysis and imaging of particulate collected from a hydrocarbon flame. The mass spectra and subsequent analysis reveal that the particulate is comprised predominately of medium ( $\approx 300$ – $800$  Da), highly condensed structures.

Additional insight to PAH structure in these measurements is found in the application of chemical graph theory. The vast majority of species observed in the sampled particulate matter are consistent with fully benzenoid morphology, consisting of fused 6-membered rings. Further, within a group of molecules with a common number of aromatic rings, species with low Dias Parameters dominate the observed spectra, despite the fact that low  $d_s$  molecules have fewer isomeric structures and this observation is more pronounced as the number of rings increases. This observation reinforces the importance of resonant stability in observed PAH distributions. Finally, CGT analysis provides clear evidence for the presence of radical PAH in the particulate samples and suggests the dominance of highly condensed aromatic structures in flame particulate.

## Experimental Section

**Experimental Details.** A 60% ethylene in nitrogen-fueled, co-axial diffusion flame was investigated in this work, where the fuel/nitrogen mixture enters from a central fuel nozzle surrounded by a concentric flow of air. This flame system has been studied extensively by our group and others using several experimental techniques, including laser induced incandescence (LII), TEM, Raman spectroscopy, and light extinction, along with corresponding computational models.<sup>[7b,8,41]</sup> In this work, particulate from the flame was thermophoretically sampled onto silicon wafer substrates. The substrates were inserted into the center of the axially symmetric flame, and the resulting deposition pattern provided a map of soot composition that may be compared with radial distribution of molecular and condensed-phase species measured by other techniques (Figure 2). Some asymmetry is observable between the left and right sides of the flame. This may be due to small differences introduced during the thermophoretic sampling in that as the sampling substrate is inserted its “left” side of the substrate is exposed to both soot growth regions of the flame whereas the “right” side is only exposed to one. Additionally, the temperature of the substrate’s left side may be higher due to a longer flame exposure, which may have an effect on thermophoretic deposition. After sampling, the wafers were analyzed by laser desorption ionization (LDI)-mass spectrometry (MS) imaging with a mass spectrometer capable of high mass resolution and accurate mass measurements. It is

important to note that a significant difference between molecular beam (MB)MS and LDI-MS techniques in the measurement of soot is that the material phase is different (gas and condensed, respectively). This difference results in low-mass PAH being undetectable in this work due to their volatility under our analytical conditions. The speciation of these lower mass compounds has been reported by several prior investigations.<sup>[13,42]</sup> Vertical sampling accuracy was limited to  $\approx 5$  mm due to instability in the sampling rig, whereas radial information is limited by the raster pitch of the subsequent LDI-MS analysis (200  $\mu\text{m}$ ) as well as profile-broadening that might occur during sampling.

The ability of LDI-MS to provide chemical information was investigated at a range of laser fluences and with soot captured on several substrates.<sup>[43]</sup> For all substrate materials, the resulting LDI-MS spectra varied with flame position and analytical conditions. Low-fluence interrogation of samples on silicon wafer substrates yielded the most artifact-free spectra. Artifacts observed with higher fluence and on other substrates include hydrogen losses from parent ions and the formation of dimers, as verified by analysis of pure PAH standards. A spectrum acquired at low laser fluence from soot captured on silicon 20 mm above the burner surface in the wing of the flame is shown in Figure 2 A. This flame area lies between the region rich in hydrocarbon intermediates formed directly from the fuel ethylene<sup>[10]</sup> and the high-temperature, radical-rich region. The highest particulate concentrations are observed in these annular regions low in this flame, here illustrated by measured laser-induced incandescence profiles of soot (Figure 2 B).<sup>[11]</sup>

Prior laser-based MS measurements resulted in only carbon cluster ions being observed in high soot regions.<sup>[44]</sup> Our PAH distribution is centered at higher mass values than previously reported MBMS or early LMMS results. In addition to the sampling method, the two most significant differences between the current study and others are the low laser fluence ( $3.2 \text{ mJ cm}^{-2}$ ) combined with a more sensitive, and higher-resolution imaging mass spectrometer. In one past report, substantially higher laser fluences were used for LDI. For example, in one manuscript, substantially higher fluences ( $> 40 \text{ mJ cm}^{-2}$ ) were needed to generate sufficient ion signal for detection.<sup>[13]</sup> Given the artifacts introduced by elevated fluences observed with PAH standards (dimerization and dehydrogenation), it is likely that reduced fluences provide better characterization of the captured material. The high mass resolving power of the Orbitrap analyzer allows for the resolution of nearly-isobaric species. This, combined with accurate  $m/z$  measurements improved by internal calibration to previously identified PAH ions, allows for the confident assignment of molecular formulae.

## Acknowledgements

The authors would like to thank Jennifer A. Giaccai for helpful discussions and Monica M. Flores for helping with experimental logistics. Partial support for this project was provided by the National Science Foundation CBET program through grants CBET-0828950, CBET1142284, and CBET-1706757 with Drs. Song Charng-Kong, Arvind Atreya, Ruey-Hung Chen, and Harsha Chelliah serving as Technical Monitors.

## Conflict of interest

The authors declare no conflict of interest.

**Keywords:** black carbon · laser desorption ionization · mass spectrometry · polynuclear aromatic hydrocarbons · soot

**How to cite:** *Angew. Chem. Int. Ed.* **2020**, *59*, 4484–4490  
*Angew. Chem.* **2020**, *132*, 4514–4520

- [1] L. J. Allamandola, A. G. G. M. Tielens, J. R. Barker, *Astrophys. J. Suppl. Ser.* **1989**, *71*, 733–775.
- [2] P. R. Buseck, K. Adachi, A. Gelencsér, É. Tompa, M. Pósfai, *Atmos. Chem. Phys. Discuss.* **2012**, *12*, 24821–24846.
- [3] Ü. Ö. Köylü, G. M. Faeth, T. L. Farias, M. G. Carvalho, *Combust. Flame* **1995**, *100*, 621–633.
- [4] M. Frenklach, *Phys. Chem. Chem. Phys.* **2002**, *4*, 2028–2037.
- [5] M. Alfè, B. Apicella, R. Barbella, J. N. Rouzaud, A. Tregrossi, A. Ciajolo, *Proc. Combust. Inst.* **2009**, *32*, 697–704.
- [6] M. L. Botero, E. M. Adkins, S. González-Calera, H. Miller, M. Kraft, *Combust. Flame* **2016**, *164*, 250–258.
- [7] a) E. M. Adkins, J. H. Miller, *Phys. Chem. Chem. Phys.* **2017**, *19*, 28458–28469; b) E. M. Adkins, J. H. Miller, *Phys. Chem. Chem. Phys.* **2015**, *17*, 2686–2695; c) E. Adkins, J. Giaccai, J. Miller, *Proc. Combust. Inst.* **2019**, *37*, 903–910.
- [8] J. D. Herdman, B. C. Connelly, M. D. Smooke, M. B. Long, J. H. Miller, *Carbon* **2011**, *49*, 5298–5311.
- [9] E. M. Adkins, J. A. Giaccai, J. H. Miller, *Proc. Combust. Inst.* **2017**, *36*, 957–964.
- [10] K. C. Smyth, J. H. Miller, R. C. Dorfman, W. G. Mallard, R. J. Santoro, *Combust. Flame* **1985**, *62*, 157–181.
- [11] M. D. Smooke, M. B. Long, B. C. Connelly, M. B. Colket, R. J. Hall, *Combust. Flame* **2005**, *143*, 613–628.
- [12] R. A. Dobbins, *Combust. Flame* **2002**, *130*, 204–214.
- [13] R. A. Dobbins, R. A. Fletcher, H. C. Chang, *Combust. Flame* **1998**, *115*, 285–298.
- [14] K. O. Johansson, T. Dillstrom, M. Monti, F. El Gabaly, M. F. Campbell, P. E. Schrader, D. M. Popolan-Vaida, N. K. Richards-Henderson, K. R. Wilson, A. Violi, H. A. Michelsen, *Proc. Natl. Acad. Sci. USA* **2016**, *113*, 8374–8379.
- [15] Q. Wang, P. Elvati, D. Kim, K. O. Johansson, P. E. Schrader, H. A. Michelsen, A. Violi, *Carbon* **2019**, *149*, 328–335.
- [16] K. H. Homann, *Angew. Chem. Int. Ed.* **1998**, *37*, 2434–2451; *Angew. Chem.* **1998**, *110*, 2572–2590.
- [17] a) A. G. Marshall, R. P. Rodgers, *Proc. Natl. Acad. Sci. USA* **2008**, *105*, 18090; b) S. M. Miladinović, V. De Vriendt, S. A. Robotham, F. Maseri, S. Lucas, C. L. Wilkins, *J. Am. Soc. Mass Spectrom.* **2010**, *21*, 411–420.
- [18] J. B. Birks, *Photophysics of Aromatic Molecules*, Wiley-Interscience, New York, **1970**.
- [19] F. Cataldo, O. Ori, M. V. Putz, *ECS Trans.* **2018**, *26*, 535–544.
- [20] a) R. Whitesides, M. Frenklach, *J. Phys. Chem. A* **2010**, *114*, 689–703; b) A. Raj, M. Celnik, R. Shirley, M. Sander, R. Patterson, R. West, M. Kraft, *Combust. Flame* **2009**, *156*, 896–913; c) M. Commodo, K. Kaiser, G. De Falco, P. Minutolo, F. Schulz, A. D'Anna, L. Gross, *Combust. Flame* **2019**, *205*, 154–164.
- [21] A. Cayley, *London Edinburgh Philos. Mag. J. Sci.* **1857**, *13*, 172–176.
- [22] M. Randić, *Chem. Rev.* **2003**, *103*, 3449–3606.
- [23] a) J. R. Dias, *J. Mol. Struct. THEOCHEM* **1986**, *137*, 9–29; b) J. Dias, *J. Mol. Struct.: THEOCHEM* **1986**, *137*, 9–29.
- [24] J. Brunvoll, S. Cyvin, *Z. Naturforsch. A* **1990**, *45*, 69–80.
- [25] S. E. Stein, A. Fahr, *J. Phys. Chem.* **1985**, *89*, 3714–3725.
- [26] a) M. Frenklach, D. W. Clary, W. C. Gardiner, S. E. Stein, *Symp. Combust. [Proc.]* **1985**, *20*, 887–901; b) J. H. Miller, *Symp. Combust. [Proc.]* **1991**, *23*, 91–98.
- [27] J. R. Dias, *Polycyclic Aromat. Compd.* **2014**, *34*, 177–190.
- [28] J. Y. W. Lai, P. Elvati, A. Violi, *Phys. Chem. Chem. Phys.* **2014**, *16*, 7969–7979.
- [29] N. Hansen, M. Schenk, K. Moshhammer, K. Kohse-Höinghaus, *Combust. Flame* **2017**, *180*, 250–261.
- [30] L. T. Scott, *Chem. Soc. Rev.* **2015**, *44*, 6464–6471.
- [31] J. Brunvoll, S. J. Cyvin, *Z. Naturforsch. A* **1990**, *45*, 69.
- [32] a) K. O. Johansson, F. El Gabaly, P. E. Schrader, M. F. Campbell, H. A. Michelsen, *Aerosol Sci. Technol.* **2017**, *51*, 1333–1344; b) K. O. Johansson, M. P. Head-Gordon, P. E. Schrader, K. R. Wilson, H. A. Michelsen, *Science* **2018**, *361*, 997; c) H. Wang, *Proc. Combust. Inst.* **2011**, *33*, 41–67.
- [33] J. H. Miller, K. C. Smyth, W. G. Mallard, *Symp. Combust. [Proc.]* **1985**, *20*, 1139–1147.
- [34] T. S. Totton, A. J. Misquitta, M. Kraft, *Phys. Chem. Chem. Phys.* **2012**, *14*, 4081–4094.
- [35] J. H. Miller, *Proc. Combust. Inst.* **2005**, *30*, 1381–1388.
- [36] R. A. Krueger, G. Blanquart, *Phys. Chem. Chem. Phys.* **2019**, *21*, 10325–10335.
- [37] G. Vitiello, G. De Falco, F. Picca, M. Commodo, G. D'Errico, P. Minutolo, A. D'Anna, *Combust. Flame* **2019**, *205*, 286–294.
- [38] H. Wang, *Proc. Combust. Inst.* **2011**, *33*, 41–67.
- [39] J. W. Martin, D. Hou, A. Menon, L. Pascazio, J. Akroyd, X. You, M. Kraft, *J. Phys. Chem. C* **2019**, *123*, 26673–26682.
- [40] a) J. Happold, H.-H. Grotheer, M. Aigner, *Rapid Commun. Mass Spectrom.* **2007**, *21*, 1247–1254; b) F. Carbone, A. Lambe, J. Jayne, D. Worsnop, A. Gomez, *Proc. Combust. Inst.* **2018**, *37*; c) F. Carbone, M. R. Canagaratna, A. T. Lambe, J. T. Jayne, D. R. Worsnop, A. Gomez, *Proc. Combust. Inst.* **2019**, *37*, 919–926.
- [41] a) B. C. Connelly, B. A. V. Bennett, M. D. Smooke, M. B. Long, *Proc. Combust. Inst.* **2009**, *32*, 879–886; b) N. J. Kempema, M. B. Long, *Combust. Flame* **2016**, *164*, 373–385; c) N. J. Kempema, B. Ma, M. B. Long, *Appl. Phys. B* **2016**, *122*, 232; d) B. Ma, M. B. Long, *Appl. Phys. B* **2014**, *117*, 287–303.
- [42] a) A. Faccinotto, P. Desgroux, M. Ziskind, E. Therssen, C. Focsa, *Combust. Flame* **2011**, *158*, 227–239; b) N. Hansen, M. Schenk, K. Moshhammer, K. Kohse-Höinghaus, *Combust. Flame* **2017**, *180*, 250–261.
- [43] R. S. J. Golden, George Washington University (Washington DC), **2019**.
- [44] R. A. Fletcher, R. A. Dobbins, H. C. Chang, *Anal. Chem.* **1998**, *70*, 2745–2749.

Manuscript received: November 5, 2019

Accepted manuscript online: January 9, 2020

Version of record online: January 30, 2020

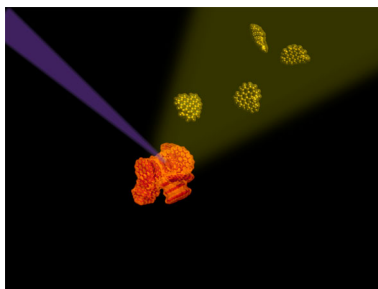
## Research Articles



## Black Carbon

R. S. Jacobson, A. R. Korte, A. Vertes,  
J. H. Miller\* ————— ■■■–■■■

The Molecular Composition of Soot



**The dominant component of soot:** Low fluence, imaging, laser desorption/ionization mass spectrometric analysis was performed on thermophoretically-sampled particulate carbon sampled from a laboratory, non-premixed flame. The data reveals that the majority of the molecular composition of soot can be characterized as fused, six-membered rings polynuclear aromatic hydrocarbons.

## Supporting Information

### **The Molecular Composition of Soot\*\***

*Rachelle S. Jacobson, Andrew R. Korte, Akos Vertes, and J. Houston Miller\**

ange\_201914115\_sm\_miscellaneous\_information.pdf

**This PDF file includes:**

Materials and Methods  
Supplementary Text  
Figs. S1 to S4  
Tables S1

## Materials and Methods

### Substrate Materials

Low resistivity (0.005-0.020  $\Omega$  cm) boron-doped p-type silicon wafers were purchased from Silicon Valley Microelectronics, Inc. (Santa Clara, CA). Wafers were  $525 \pm 25$   $\mu\text{m}$  thick and were received polished on one side. The polished side was used without further cleaning. Prior to sampling, round wafers were hand cut with a diamond pen into pieces  $\sim 1$  cm tall and  $\sim 2$  cm wide.

### Burner and Flame Specifications

The burner specifications are available through the International Sooting Flame (ISF) workshop website (<https://www.adelaide.edu.au/cet/isfworkshop/>). Briefly, the burner consisted of a vertical fuel tube (4 mm I.D.) surrounded by a concentric air co-flow (74 mm I.D.). The cold flow velocity for total fuel and oxidizer was set to 35 cm/s. In these measurements, only the 60% ethylene, 40% nitrogen dilution was used. The resulting flame was lifted  $\sim 3$  mm from the burner surface and the tip of the flame was  $\sim 5$  cm from the top of the burner. Ethylene (99.9%) and nitrogen (99.995%) gases were acquired from Roberts Oxygen (Rockville, MD). The co-flowing air was supplied by an in-house compression system.

### Thermophoretic Sampling

The thermophoretic sampling rig used in these experiments was also used in an earlier work by our group (*J*). The sampling process is enabled by a pneumatic slide (Omega Engineering, Inc., Norwalk, CT, DLM-09M-50-50-P), with a movement range of 50.8 mm. Extension and retraction are achieved by a system of solenoid and relays (Omega Engineering, Inc., Norwalk, CT, OM-Air-C2VA0045 and SSR330DC10, respectively), which are controlled by a NIDAQ (National Instruments, Austin, TX, SCB-68) via a homebuilt LabView program.

A custom machined sample holder was constructed from two stainless steel rods to hold the silicon wafer pieces directly. A schematic of the sample holder is shown in Fig. S1. A 12.7 mm diameter rod, 304 mm long, was clamped to a pneumatic slide with  $< 30$  mm extended. All sections of the sample holder to the left of the 12.7 mm rod were constructed from a solid piece of stainless steel. An identical copy of the flattened 46 mm (left) were machined from a second piece and affixed with two set screws to directly hold the silicon wafer. The total thickness of both pieces together is 1.5 mm. The silicon wafer substrates were positioned between these two plates and the screws were tightened. Due to the thickness of the silicon wafer, a small piece of wire was also used to increase the grip of the sample holder on the wafer substrates.

The pneumatic slide, clamps, and sample holder were all positioned using construction rails (Thorlabs, XE25) and an optical breadboard (Thorlabs, MB8). Video monitoring of sampling processes was achieved with a 240 fps camera; thus, the temporal resolution is limited to one frame every 4.2 ms. Sampling times were all set to 400 ms, though the total flame interaction time was  $250 \pm 36$  ms. The sampling process encompassed four distinct steps: entering the flame, vertical vibration phase, staying stationary, and exiting the flame. Average sampling times for each of these steps are  $47 \pm 6$ ,  $49 \pm 4$ ,  $89 \pm 11$ , and  $66 \pm 14$  ms, respectively.

Immediately after exposure to the flame environment, each piece of silicon wafer was taped to a commercial MALDI-MS sample plate using double-sided carbon tape (Ted Pella, Inc., Redding, CA). The carbon tape has been shown not to contribute to MS signal unless directly exposed to laser radiation, which was avoided here. Samples were exposed to air for less than

one hour. They were taken directly to the mass spectrometer source and inserted into the vacuum chamber.

### Laser Desorption Ionization Mass Spectrometry Imaging

All measurements were made on a MALDI-LTQ-Orbitrap XL mass spectrometer (Thermo Scientific, San Jose, CA) in positive ion mode. This instrument is equipped with an intermediate-pressure (75 mTorr) MALDI source, which includes a nitrogen laser emitting 337 nm light with 4 ns pulse width and a repetition rate of 60 Hz. The laser beam interacts with the sample at an angle of 32° from the normal, in the reflection geometry configuration. The laser power is precisely controlled via software and is continuously monitored, with one 50% neutral density filter in the beam path. All acquisitions were performed using 10 laser shots per spectrum. All spectra were acquired in the Orbitrap analyzer with a resolving power setting of 100,000, though the resolution is  $m/z$  dependent. Due to tradeoffs in ion transfer optics settings, the instrument loses sensitivity when an overly wide range is selected; therefore, the acquisition range was limited to  $m/z$  150-1000 after preliminary experiments confirmed no ions were observed outside that range.

Mass spectra were acquired using the control software MS imaging mode. In this mode, the sampling laser is rastered in discrete steps over the desired area and a spectrum is recorded at each of a series of  $x,y$  positions (pixels). From these spectra and the corresponding  $x,y$  positions, maps of the distribution of specific ions can be generated. The imaging step size describes the distance the sample plate moves between pixels. The laser spot is roughly elliptical (100  $\mu\text{m} \times 80 \mu\text{m}$ ), but a step size of 200  $\mu\text{m}$  was used as preliminary experiments showed no significant increase in spatial information when lower step sizes were used and features < 200  $\mu\text{m}$  were not observed.

Much attention was paid to the laser fluence used in these experiments. After extensive investigation with small PAH standards, it was determined that 0.2  $\mu\text{J}$  of laser energy, corresponding to a fluence of 3.2  $\text{mJ}/\text{cm}^2$ , delivered to the sample resulted in no significant dimerization or fragmentation on when the sample was placed on silicon wafer substrates. Only molecular ions were observed.

Silicon nanopost arrays (NAPA) were also tested as a substrate for laser desorption ionization mass (2, 3). Due to the scale of the silicon nanoposts, the thermal stability of these structures might be expected to not hold up to flame insertion. Additionally, there was no discernable difference between mass spectra recorded on flat wafers and NAPA areas. Given the highly aromatic nature of PAHs, energy from the UV laser used here is absorbed by the analytes leading to ion production without the need for an external medium or matrix.

### Data Analysis

Data was extracted from localized sample positions, representing soot from corresponding flame areas, using ImageQuest software (Thermo Scientific, San Jose, CA). Resulting spectra were imported to mMass for peak identification (<http://www.mmass.org/donate/papers.php>). A list of six PAH were used to apply a slight mass calibration, restricted to a 5 ppm mass window. After calibration, the spectral features were compared to a list of theoretical  $m/z$  values for all possible combinations of 100 carbon atoms, 100 hydrogen atoms, and up to 4 oxygen atoms. In this mass range, restricting the number of carbon and hydrogen atoms available for accurate

mass matching can bias the results leading to identified peaks with unrealistically high oxygen content (4).

### **Review of Possible Biases in Analytical Technique**

A possible concern in these measurements is potential to bias the observed ion signals to either lower or higher mass species. At the low fluence used for these measurements, however, these effects were determined to be minimized by measuring standard PAH species  $\leq 300$  Da. Additionally, low-mass PAH species ( $< 230$  Da) were not observed because of their high volatility. Analytical standards were not available for large PAH molecules to evaluate the stability of these molecules in our experiments. Previous work, however, does not suggest a significant bias away from stable, high mass molecules such as PAH larger than those observed. (5)

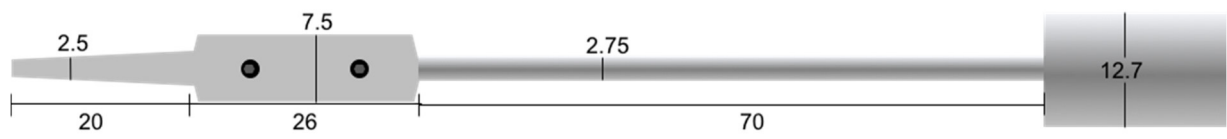


**Fig. S1.**

Schematic diagram of the substrate holder for the thermophoretic sampling process. All values are in mm. The flattened areas on the left are 1.5 mm thick in total, whereas the round rods in the center and right are cylindrical, therefore their diameters are provided.

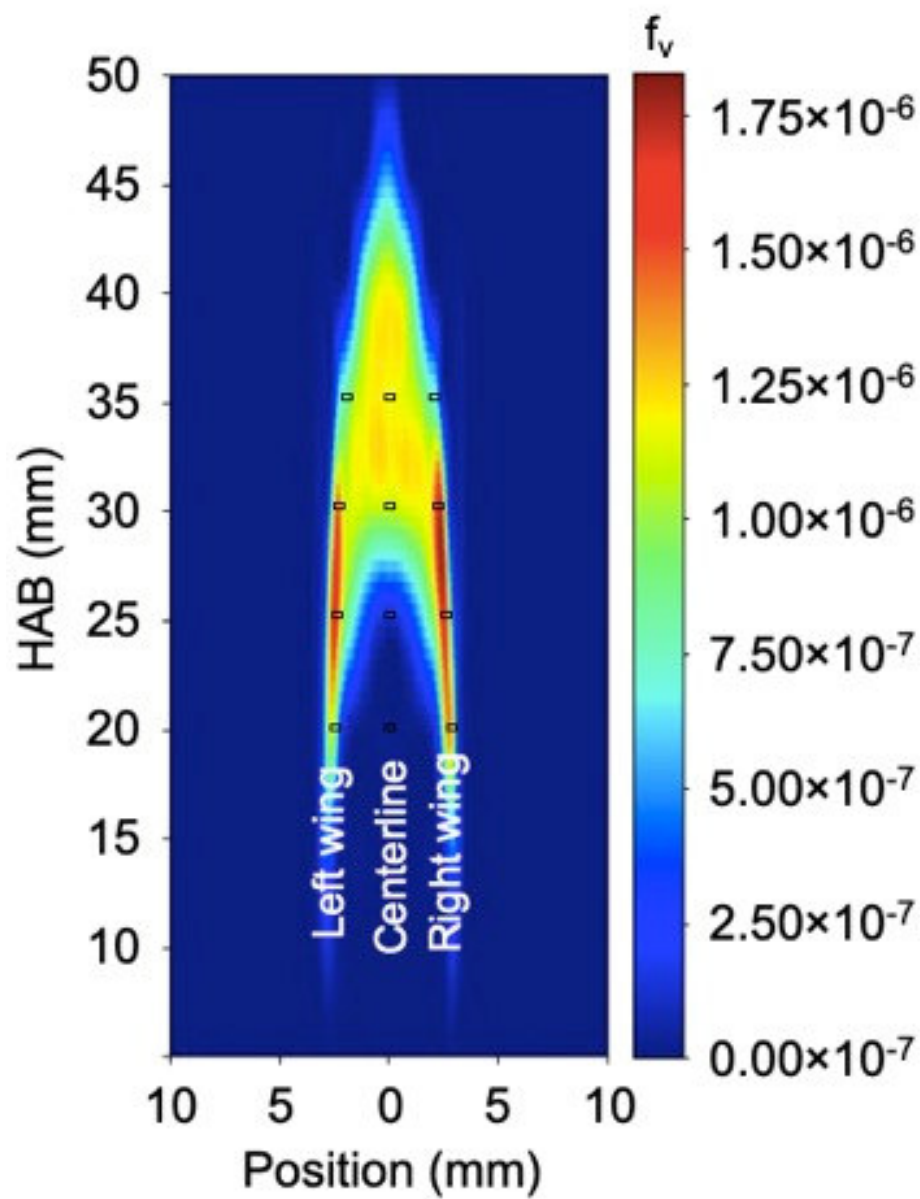
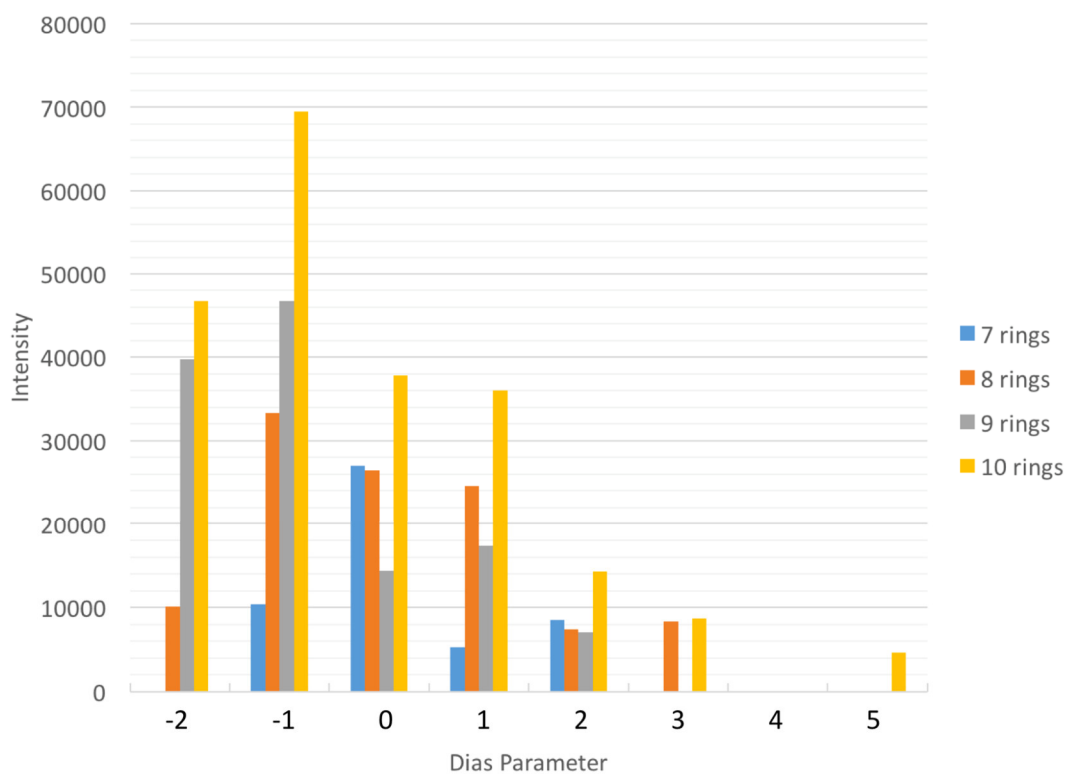
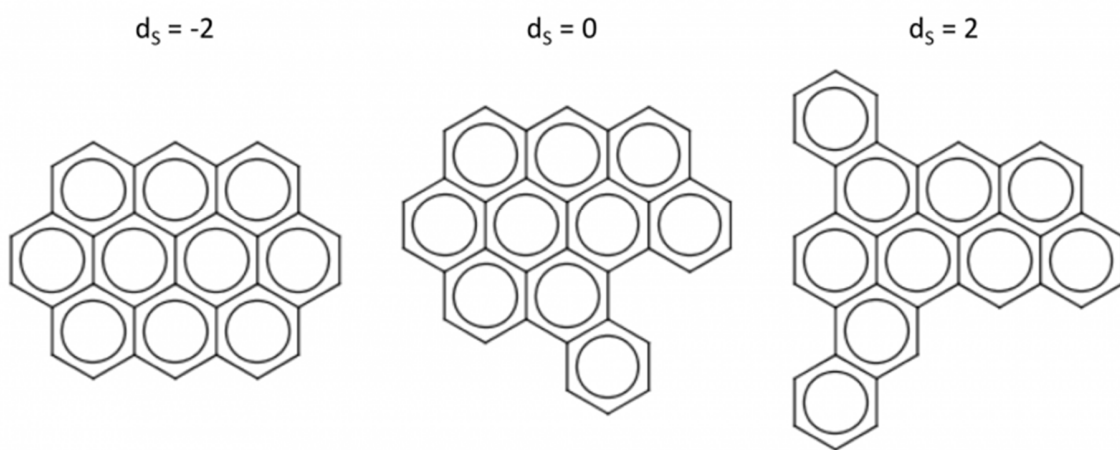


Fig. S2.

Map of sampling locations whose data is shown in the manuscript's Figure 3 superimposed on a false color image of soot particle volume fraction as determined by laser-induced incandescence (6).

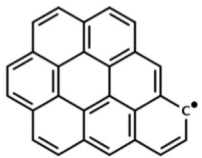
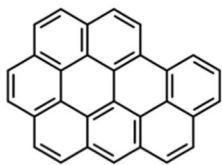
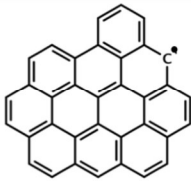
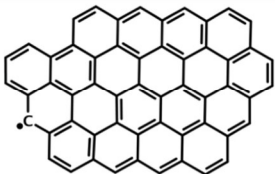


**Fig. S3**  
Laser desorption mass spectral intensity observed at 35 mm above the flame on the right “wing” as a function of Dias Parameter for selected, constant aromatic ring counts.



**Fig. S4**

Illustration of structural changes with Dias Parameter for selected 10 ring compounds. Note that there is only 1 isomer for DS= -2, 42 isomers for DS=0, and 416 isomers for DS=2.

Chemical Formula	Structure	Chemical Formula	Structure
$C_{27}H_{13}$		$C_{47}H_{17}$	
$C_{30}H_{14}$		$C_{50}H_{18}$	
$C_{35}H_{15}$		$C_{55}H_{19}$	
$C_{40}H_{16}$		$C_{60}H_{20}$	

**Table S1.**

Suggested structures corresponding to labeled MS peaks in Fig. 2. Note that the illustrated radical site on the “odd hydrogen” structures would be expected to be in resonance with several additional and equivalent structures.

## Supplemental References

1. J. D. Herdman, B. C. Connelly, M. D. Smooke, M. B. Long, J. H. Miller, A comparison of Raman signatures and laser-induced incandescence with direct numerical simulation of soot growth in non-premixed ethylene/air flames. *Carbon* **49**, 5298-5311 (2011).
2. B. N. Walker, J. A. Stolee, A. Vertes, Nanophotonic Ionization for Ultratrace and Single-Cell Analysis by Mass Spectrometry. *Analytical Chemistry* **84**, 7756-7762 (2012).
3. S. A. Stopka *et al.*, Molecular Imaging of Biological Samples on Nanophotonic Laser Desorption Ionization Platforms. *Angewandte Chemie International Edition* **55**, 4482-4486 (2016).
4. K. O. Johansson *et al.*, Formation and emission of large furans and oxygenated hydrocarbons from flames. *PNAS* **113**, 8374-8379 (2016).
5. B. Apicella *et al.*, Mass spectrometric analysis of large PAH in a fuel-rich ethylene flame. *Proc. Combust. Inst.* **31**, 547-553 (2007).
6. M. D. Smooke, M. B. Long, B. C. Connelly, M. B. Colket, R. J. Hall, Soot formation in laminar diffusion flames. *Combustion and Flame* **143**, 613-628 (2005).